

The Corrosion of Alloy 718 During 800 MeV Proton Irradiation

R.S. Lillard, G.J. Willcutt[☆], D.L. Pile[‡], D.P. Butt^{*}

Materials Corrosion and Environmental Effects Lab
Materials Science and Technology Division, MST-6
Los Alamos National Laboratory
Los Alamos New Mexico 87545

Abstract

The real-time polarization resistance of Alloy 718 during high energy proton irradiation (measured with electrochemical impedance spectroscopy) decreased from $1.7 \times 10^3 \text{ ohm} \cdot \text{m}^2$ in the absence of irradiation to $8.2 \text{ ohm} \cdot \text{m}^2$ at a proton beam current of 0.4 mA. Because the proton beam spot size was smaller than the sample (that is, proton flux decreased radially from the beam center), two methods for determining corrosion rate from polarization resistance were employed. The first method assumed that the distribution of corrosion was uniform across the entire probe surface. With this assumption, the corrosion rate was found to vary from $0.041 \times 10^{-6} \text{ m/yr.}$ at an average proton current of 0.001 mA to $3.1 \times 10^{-6} \text{ m/yr.}$ at an average proton current of 0.40 mA. The second method used proton flux as a criterion for determining the area of highest damage. At a peak proton flux of $1.77 \times 10^{18} \text{ p/m}^2 \cdot \text{s}$, calculated at an average proton current of 0.40 mA, the corrosion rate was $60.9 \times 10^{-6} \text{ m/yr.}$ These results are discussed within the context of water radiolysis and direct 718/proton interactions.

[☆]Technology, Safety and Assessments Division, TSA-10

[‡]Present address: Dept. of Materials Science, University of Virginia, Charlottesville, VA, 22903

^{*}Present address: Ceramtec Inc., 2425 South 900 West, Salt Lake City, Utah, 84119

1. Introduction

1.1. Spallation neutron sources

Spallation neutron sources typically consist of a proton accelerator (linac / synchrotron) and a shielded cavity which contains the neutron source (or target). This target is a high Z number metal, for example tungsten (W) or tantalum (Ta). High energy neutrons are produced when the proton beam leaves the high vacuum of the accelerator via a "window" and enters the cavity where it then strikes the target. Many of the components in the cavity (including the window) are constructed from or clad with Alloy 718 (UNS N07718, precipitation hardened, Cr-18 wt%, Fe-19, Nb-5, Mo-3, Ti-1, and Ni-53 min). To keep the target cool (and to moderate the energy of the neutrons which are produced) it is enclosed in a cooling loop which is generally constructed from stainless steel 304 (UNS S30400; referred to as 304 SS) and filled with deionized water, although ppb - ppm contaminants such as chloride and sulfate are typical. The cooling loop is typically operated at upwards of 2×10^6 Pa and flow rates on the order of liters per second.

In designing a spallation neutron source candidate materials and engineering designs must be chosen to minimize a number of potential corrosion related failure modes, such as pitting corrosion, galvanic corrosion, crevice corrosion, and stress corrosion cracking. In addition, materials corrosion in a spallation neutron source may also be effected by ionizing radiation. Preliminary data from irradiations at the Los Alamos Neutron Science Center (LANSCE), suggest that corrosion rate is a function of proton flux(1). Additional results from Maloy *et al* found that the post irradiation thickness profile of a W rod, irradiated at a beam current of 1.0 mA for approximately 2 months, was Gaussian and corresponded to the Gaussian profile of the beam(2, 3). Although the corrosion damage near the center of the W probe appeared to be mixed mode, the full width at half the maximum (FWHM) was approximately 3.2 cm while, the theoretical FWHM for the proton beam was 3.26 cm (Figure 1).

In addition to the effects associated with the direct interaction of the beam with materials, the design must also consider water radiolysis products that result from the interaction of ionizing radiation with water. The formation of long-lived water radiolysis products (such as H_2O_2) occurs

from the recombination of short-lived radiolysis products (such as OH) that have lifetimes on the order of 10^{-12} to 10^{-6} seconds. While the effect of the short-lived products on corrosion rates is unknown, radiolysis products such as H_2O_2 are cathodic reactants and increase open circuit potentials (OCP) and corrosion rates (in cathodically limited reactions) of metals. Therefore, in addition to the potential failure modes discussed above, the corrosion of materials in neutron source cooling loops may be accelerated by both long lived and short lived water radiolysis products. While water dissociation is unavoidable, the formation of long-lived products can be suppressed. For example, dissolved hydrogen will suppress OH/OH recombination and H_2O_2 formation. A thorough discussion of the effects of water radiolysis on corrosion and mitigation methodology will be presented in future publications.

Because the post irradiation examination of samples must be conducted in a hot cell, weightloss and thickness measurements are a costly and time consuming way of measuring corrosion damage caused by proton irradiation. In addition, for corrosion resistant materials, such as Alloy 718, where the corrosion rate may be on the order of 10's $\mu\text{m}/\text{year}$ of irradiation, these methods are ineffective in determining corrosion rate after short irradiation periods. The purpose of this paper is to determine the "real-time" corrosion rate of Alloy 718 during high energy proton irradiation; that is, to determine the effect of the direct interaction between energetic particles and the metal corrosion rate. To accomplish this, a method for measuring the real-time corrosion rate of metals during 800 MeV proton irradiation is necessary.

1.2. Effects of proton irradiation on corrosion

There have been a limited number of studies which have addressed the corrosion behavior of metals in high energy particle beam environments. None have measured the real-time corrosion of metals in a particle beam. Simnad and Smoluchowski measured the circuit potential (OCP) of a tungsten target as a function of proton fluence in an 260 MeV proton beam(4). The sample was a 0.3 mm diameter tungsten wire which was annealed at 900° C and degreased before being placed in an irradiation cell. The electrolyte was an oxygen-free, saturated KCl solution. The OCP of this target was measured during irradiation with respect to a saturated calomel electrode by means of a

vacuum tube potentiometer. They found that the OCP of the tungsten target became more positive with increasing proton fluence as shown in Table 1. Their interpretation of this result was that particle radiation created defects at the metal surface which contributed to the observed increase in electrode potential. They theorized that the defects had to be large (dislocation lines, loops, or collapsed vacancy clusters) because isolated vacancies and interstitials would presumably disappear rapidly given their proximity to the surface. In order to test the hypothesis that defects at the metal surface were responsible for the observed change in potential, they first irradiated a sample while monitoring its OCP. After the irradiation period the sample was annealed at 900° C. After the annealing period they measured the electrode potential of the W sample out-of-beam and found that it had returned to its original value. They concluded that the damage was reversible as it could be "baked out".

A similar study on the proton irradiation of iron addressed metal dissolution rate(5). In this study an iron electrode was immersed in a pH 2, HCl solution. Weight loss measurements found that, for a fluence of 1×10^{20} protons/m², the corrosion rate increased from 4 g/m² in the absence of irradiation to approximately 14 g/m² during irradiation.

Investigators have also evaluated the efficacy of corrosion inhibitors in particle accelerator cooling loops(6). These studies focused on the addition of hydrazine and benzotriazole (an anodic inhibitor) at the CERN accelerator to mitigate copper corrosion in the magnet cooling water loops of the synchrotron. The corrosion rate of copper during 600 MeV irradiation decreased in the presence of both inhibitors (evaluated by the concentration of Cu⁺⁺ in solution). However, radiolytic decomposition of the inhibitors was noted at low radiation flux (2.5×10^{11} p/m²•s). Future spallation neutron sources are likely to have much higher proton flux (5.5×10^{16} p/m²•s), although the application of inhibitors may play a role in secondary cooling loops where aluminum alloys are present.

2. Experimental

2.1. The in-beam corrosion loop

All experiments were conducted at the A6 Target Station of LANSCE which is located in Experimental Area A just in front of the linac beam stop at the Los Alamos National Laboratory. A detailed description as well as diagrams of the beam at A6 have been presented elsewhere(7). Briefly, the corrosion water loop at LANSCE consisted of a pumping system and a manifold which held the corrosion samples in-beam (Figure 2). With the exception of the corrosion probes, the system was fabricated entirely of 304 SS (it is recognized that stainless steel 308 weld rods were used in the welding of 304 SS components).

To measure real-time in-beam corrosion rates, it was necessary to electrically isolate the Alloy 718 corrosion samples from the stainless steel plumbing system. Conventionally, this can be accomplished with metal-to-glass seals. However, proton irradiation of glass causes it to become relatively conductive, rendering the electrical insulating properties of the seal useless. Therefore, an alternate sealing method was designed. As shown in Figure 3a, the in-beam corrosion samples were hollow rods (one end closed, one end open) with an outside diameter of 1.27 cm and a length of 15.9 cm. The wall thicknesses varied with sample material type. The Alloy 718 sample had wall thickness of 0.32 cm. The inner diameter of the manifold tube that housed the Alloy 718 sample was 1.73 cm, therefore, the annulus spacing between the sample and the tube (where the water coolant flowed) was 0.23 cm. By varying the wall thickness of the samples, the surface temperature of each sample (during irradiation) could be kept at a target value. The open end of the sample was joined to one end of a dumb-bell shaped ceramic (alumina) by means of a compression seal. The other end of the ceramic was joined to a stainless steel 304L (304L SS) flange by means of another compression seal. The flange provided a means for welding the probe assembly into a water manifold. Electrical contact to the sample was made via a nickel wire which was spot welded to the inside of the probe prior to joining and fed through a hole in the ceramic. The ceramic sealing process required the corrosion samples to be held at

approximately 800-900° C for 10 to 20 minutes. Similar heat treatment of Alloy 718 in the lab showed no substantial microstructural differences as compared to the as received material.

The water manifold (Figure 3b) consisted of seven 20 cm long tubes arranged in a close-packed array. Each tube contained either an in-beam corrosion probe described above, a set of stress corrosion cracking samples, or a weightloss specimen. The manifold was welded to the bottom of an 3.4 m supporting insert which not only supported the weight of the manifold but also provided the necessary conduits for electrical and water connections. Thermocouples attached to the front of the manifold verified the position, size, and shape of the proton beam. A diagram depicting the corrosion insert (insert 17B) and its relative position at the target station is presented in Figure 4.

In addition to the in-beam probes, samples were also located out-of-beam, upstream and downstream from the manifold; a considerable distance from any proton or neutron flux (see supply/return side corrosion probes in Figure 2). The probes which held these samples were purchased off-the-shelf from a commercial vender and allowed the real-time polarization resistance of samples to be measured. They employed glass-to-metal seals. These out-of-beam probes held samples of aluminum alloys 6061 and 5052, W, tantalum, 304L SS, 316L-NG SS, and Alloy 718. Complete results from these probes will be reported in future papers.

2.2. Sample preparation and water quality

To provide a fresh metal surface for electrochemical characterization, all samples were ground to 400 grit using SiC paper. After grinding, the samples were degreased in an ultrasonic bath of acetone. Degreasing was followed by successive ultrasonications in ethanol and de-ionized water.

Prior to placing the probes in the water system, the interior of the system which included all piping, tanks, and pumps was steam cleaned and rinsed with a mixture of water and ethanol. The water system was then filled with DI water (approximately 230 liters), operated for several hours and then flushed. This was repeated three times before the final system fill with DI water. The water resistivity varied between 1×10^6 ohm cm (initial) and 8×10^4 ohm cm (after several weeks of

operation). Ion coupled plasma analysis of a water sample taken from the system prior to irradiation found: 5.4×10^{-5} mole/m³ W, 1.2×10^{-3} mole/m³ magnesium, 1.8×10^{-4} mole/m³ iron, 6.1×10^{-4} mole/m³ zinc, 3.1×10^{-4} mole/m³ copper, and 0.064 mole/m³ calcium. The zinc, copper, and calcium impurities likely owed to insufficient de-ionization of the source water. Nominally, the system operated at a water temperature of approximately 20° C +/- 5, a pressure of 0.86×10^6 Pa, and a total flow rate of 1.0 L/s. This resulted in a flow rate of 0.095 L/s at the probes, a water velocity of approximately 0.95 m/s in the annulus between the samples and the tube wall, and a Reynolds number of 4860 (calculated at 20° C). In an attempt to mitigate the formation of water radiolysis products such as H₂O₂ (6-10), the system was operated with a dissolved hydrogen concentration of approximately 0.40 mole/m³. This was accomplished by continuously bubbling 6% H₂ - 94% Ar gas into the system's reservoir tank. Dissolved hydrogen concentration was measured with an Orbisphere TCD Hydrogen analyzer. A thorough discussion of the effects of water radiolysis on corrosion and mitigation methodology will be presented in future publications.

2.3. Proton beam characteristics

The flux of the incident proton beam had a Gaussian distribution of 2 – 3 cm. The energy of this particle beam was 800 MeV. The beam had a characteristic macropulse repetition rate of 100 Hz, a gate length of 835 microseconds, and a fixed peak current of 16 mA (Figure 5). Average proton beam currents were controlled by varying the spacing between each micropulse (and therefore the number of micropulses) in the gate as well as the repetition rate. Nominally, the average proton beam currents varied between 0.001 and 0.40 mA. Although the beam may be characterized in terms of current density (charge per unit area per unit time) these particles are ballistic in nature and are not to be confused with electrical current in EIS. Moreover, because of their energy virtually 100% of the particles striking the corrosion samples pass through.

2.4. Electrochemical measurements

Electrochemical impedance spectroscopy (EIS) was used to measure the polarization resistance of each sample as a function of beam current and irradiation time(8-10). To maximize the signal-to-noise ratio measurements were conducted with a 30 mV peak-to-peak sinusoidal

voltage perturbation over the frequency range of 0.005 - 1000 Hz. No applied dc potential was employed; that is, all measurements were conducted at the OCP. To eliminate the effects of ground loops, a floating ground EIS system was used. Because a traditional reference electrode was not capable of withstanding the proton / neutron flux at the manifold, a two electrode EIS measurement was employed for all in-beam experiments. In the two electrode in-beam measurement the water system (ground) acted as both reference and counter electrodes. In this measurement the counter electrode interface can be neglected because of the large surface area of the 304 SS water system and its relatively unchanging potential as measured with a reference electrode downstream. That is, although the polarization resistance of the 304 SS system was large ($>100 \text{ ohm} \cdot \text{m}^2$) its surface area was also large. As a result its contribution to the measured resistance was small (less than 20 ohms). The validity of this method was confirmed by comparing the pre-irradiation EIS results from the Alloy 718 in-beam probe with those from the Alloy 718 out-of-beam samples. Out-of-beam EIS measurements were conducted in the traditional three electrode configuration with a tungsten / tungsten oxide electrode serving as the reference and an isolated Alloy C276 sample as the counter electrode. The area normalized polarization resistance for both the out-of-beam and in-beam Alloy 718 samples prior to irradiation were identical.

Initial irradiation experiments were conducted during proton irradiation at average proton beam currents of 0.001, 0.010, 0.04, 0.10, and 0.40 mA. That is, electrochemical measurements were conducted while the proton beam was on. These data were taken with all other inserts (17A - 18C in Figure 3) pulled out of the proton beam path such that the first material that the proton beam struck after leaving high vacuum the most forward tube of the corrosion manifold. After approximately 300 hrs of experiments with only the corrosion insert in place, inserts 17A, 18A, 18B, and 18C were placed in position in front of the corrosion insert and the beam current was increased to 1.0 mA. The effect of these inserts in front of the corrosion insert was to spread the

Although a 30 mV perturbation is somewhat higher than that typically used in EIS measurements (10 mV), for metals undergoing passive dissolution (as is the case for alloy 718 in DI water) the effect of an applied anodic voltage is to thicken the passive film. However this increase is small (for aluminum the passive film grows 1.4 nm/V). Therefore, no appreciable effect of a 30 mV peak-to-peak perturbation on sample is anticipated.

proton beam from its compact Gaussian distribution to a more diffuse, cloud-like beam. That is, for any given current the beam flux at the corrosion insert was lower with the forward inserts in place. Interaction of the beam with the materials in the forward inserts also increase the neutron flux at the corrosion insert.

3. Results

3.1. Effect of proton irradiation on polarization resistance

Upon turning the proton beam on, a sharp increase in OCP of Alloy 718 was always observed (Figure 6). Correspondingly, no change in the OCP of the downstream sample was observed. Upon turning the beam off, a sharp decrease in the OCP of the in-beam sample was observed followed by a more gradual decrease back to the original OCP (data not shown). Typical EIS data from an Alloy 718 in-beam corrosion sample (with the beam on) as a function of proton beam current are presented in Figure 7 in the form of Bode magnitude (7a) and phase plots (7b). The magnitude of the impedance has been normalized for area by multiplying $|Z|$ by the total sample area. Because the proton beam spot size was small relative to the total probe area, this assumption is non-conservative. Therefore, this will be referred to as the uniform polarization resistance. The topic of area normalization as it pertains to corrosion rate will be addressed later in this paper. Because only one time constant was observed in the EIS data, the simplified Randles equivalent circuit(11) (EC) shown in Figure 8a was chosen to model the data. In this circuit: R_{pol} is the polarization resistance, C_{dl} is the capacitance associated with the double layer, and R_{sol} is the geometric solution resistance between the sample and the water system. A complex non-linear least squares (CNLS) fit of the in-beam data at a proton current of 0.40 mA to this EC is presented in Figure 9. As seen in this figure, good agreement between the model and the data exists. The uniform polarization resistances ($R_{pol} \times \text{total area in } \text{ohm} \cdot \text{m}^2$) obtained from CNLS fitting as a function of proton beam current are presented in Figure 10. An exponential decrease in uniform polarization resistance with increasing beam current was observed. Here, we have chosen to plot uniform polarization resistance as a function of proton beam current as it includes the effects of

proton fluence, flux, and water radiolysis on corrosion rate. The topics of proton flux, fluence and water radiolysis are addressed individually below.

To determine whether or not the interaction of the proton beam with the metal produces a steady state condition which does not change once the sample is removed from the proton beam, EIS data were collected before irradiation, during irradiation at 40 μA , immediately after irradiation at 0.04 mA (referred to as "instant off"), and 3 hrs after irradiation at 0.04 mA. In an attempt to collect as much "near dc" data as rapidly as possible, the instant off data were only collected between the frequencies of 0.10 and 0.01 Hz which resulted in a minimal 20 minute measurement time. As seen in Figure 11 the magnitude of the impedance ($|Z|$) at low frequencies was lower during irradiation at 0.04 mA than before irradiation. The impedances measured immediately after the beam was turned off were somewhat higher than those measured during irradiation. Approximately 3 hours after irradiation the low frequency impedance was found to returned to the pre-irradiation level. These findings are evidence that the effect of proton irradiation on corrosion rate decays with time after the beam is shut off. It may also be noted that the slopes of the 0.04 mA data and pre/post irradiation plots between 0.03 and 1.0 Hz are equal to -1, as anticipated for steady state capacitive behavior (Figure 8a). For the instant off measurement, the data has a slope greater than -1. This behavior is indicative of a changing system, that is, the instant off data was non-steady state as the probe's response became more post-irradiation-like (and consequently less in-beam like) with increasing time after the beam was turned off. It is also apparent from Figure 11 that proton fluence is not the controlling parameter as the pre-irradiation and post-irradiation corrosion rates were identical. This topic will be addressed in greater detail in following sections.

3.2. Corrosion rate calculations

Because the beam spot was small relative to the size of the Alloy 718 corrosion sample (the beam width at 2 was equal to 3 cm vs. probe dimensions of 1.3 cm in diam. x 15.9 cm in length) and, therefore, the proton flux varied across the sample surface, two methods for determining corrosion rate from R_{pol} were derived. The first method used proton flux (from the incident proton beam) as a criterion for determining the area of highest damage. The proton flux profile of the

beam at LANSCE A6 has been characterized and found to have a Gaussian distribution rotated about a central axis(12). The relationship between proton flux and radial position from the center of the beam is given by:

$$j_r = j_0 \exp\left\{-\frac{r^2}{2\sigma^2}\right\} \quad (1)$$

where: j_r is the flux in $\text{p/m}^2 \cdot \text{s}$ or $\mu\text{A/m}^2$, r is the distance from the center of the beam in m, and σ is the standard deviation of a Gaussian distribution in m. For j_r (the flux at $r=0$) in mA/m^2 j_0 is given by:

$$j_0 = \frac{I_t}{2\sigma^2} \quad (2)$$

where I_t is equal to the average beam current in mA. For our study 2σ was equal to approximately 0.003 m ($\sigma = 1.5$ cm) and I_t was varied from 0.001 to 0.40 mA as discussed above. Assuming that corrosion occurs preferentially in the beam and is proportional to proton flux, a relationship between polarization resistance and proton flux can then be established from equation 1:

$$R_{\text{pol}}^G = \frac{b}{j_0 \exp\left\{-\frac{r^2}{2\sigma^2}\right\}} \quad (3)$$

where R_{pol}^G is the area normalized Gaussian distribution of the polarization resistance in $\text{ohm} \cdot \text{m}^2$. The constant, **b**, has units of $\text{ohm} \cdot \text{m}^2 \cdot \mu\text{A}$ and was determined by fixing the average polarization resistance (\bar{R}_{pol} in $\text{ohm} \cdot \text{m}^2$) to an area defined by 2σ (d) where d is the sample diameter in m:

$$\bar{R}_{\text{pol}} = R_{\text{pol}} \cdot 2\sigma \quad (d) \quad (4)$$

$$b = \bar{R}_{pol} \exp \left(-\frac{r^2}{2} \right) \quad (5)$$

where R_{pol} is in units of ohms and is obtained from CNLS fitting of the EIS data as discussed above.

From R_{pol}^G , the corrosion rate (CR) in 10^{-6} m/yr., was determined as a function of position as seen in Figure 12 from the well know relationship:

$$CR = \frac{327.6 \left(26 / R_{pol}^G \right) (EW)}{\quad} \quad (6)$$

where ρ is the density of Alloy 718 and is equal to 8.19×10^3 kg/m³, the units conversion constant 327.6 has units of (kg·μm)/(m·mA·yr.), and EW is the equivalent weight of Alloy 718 and is equal to 25.66 (dimensionless). The constant 26 in Eq. 6 assumes Tafel slopes of 0.12 V/decade. The error associated with this assumption is small and has been addressed elsewhere(13). As may be anticipated, the highest corrosion rates are found at the center of the probe (at $r=0$). It should be noted that the theoretical r^2 for a the proton beam is in close agreement with r^2 in the corrosion rate distribution (3.1 cm). A plot of corrosion rate as a function of proton flux (from the incident proton beam) is presented in Figure 13. As seen in this plot, at an average proton current of 0.04 mA the calculation predicts that the corrosion rate of Alloy 718 is 4.7×10^{-6} m/yr. at a proton flux of 1.8×10^{17} p/m²·s. However, at an average proton current of 0.40 mA the model predicts that the corrosion rate is 2.5×10^{-6} m/yr. for the same proton flux. This may be a limitation of the assumptions in the calculation, however, it is more likely an indication that there are factors other than the incident proton flux that contribute to the measured corrosion rate. Future experiments will focus on the role of gate length, repetition rate, peak proton current, and total radiation flux (photo + neutron + proton) on corrosion rate. Specifically, to verify the damage distribution predicted in Figure 13, corrosion probes of the same material will be placed at various radial

distances from the proton beam. The data from these probes will be compared to radiation transport code (LAHET) calculations of the total proton, neutron, and photon flux distribution.

For comparison, calculations were also performed that assumed corrosion rate was independent of proton flux. Specifically, the distribution of corrosion was assumed to be uniform across the entire probe surface. To calculate corrosion rate, the uniform polarization resistance (Figure 10) was used in Eq. 6 in place of R_{pol}^G . That is, R_{pol} from CNLS modeling of the EIS data was multiplied by the total probe area (approximately $6.34 \times 10^{-3} \text{ m}^2$). The results are presented in Figure 14. For comparison, the peak corrosion rates at $r=0$ (that is at the peak flux) from the Gaussian flux distribution are also presented. The assumption that corrosion rate is uniform across the entire sample surface is non-conservative and should be considered the minimum rate. The change in corrosion rate as a function of beam current was similar for both assumptions and can be defined by the relationship:

$$\log(\text{CR}) = \quad + 0.68 \log(\text{BC}) \quad (7)$$

where BC is beam current in mA and \quad is a constant and is dependent on the method used to calculate corrosion rate. The values for \quad are: 0.25 and -0.68 for the Gaussian and uniform polarization resistance assumptions, respectively. Nearly identical results were obtained for two additional Alloy 718 probes in subsequent irradiations(14).

3.3. The effect of proton fluence on corrosion rate

In addition to measurements with only the corrosion insert in-beam, measurements were also made over several months with the four other inserts (17A and 18A-C) in front of 17B. These measurements were conducted at a proton beam current of 1.0 mA. The polarization resistance of Alloy 718 as a function of the calculated proton fluence[†] is presented in Figure 15. As before, all

[†] Calculated by integrating Equation 1 over time. The decrease in flux due to the forward inserts at $I_t=1.0\text{mA}$ was corrected for by using 0.4 mA as the average current during the period of time that the forward inserts were in place. This may have resulted in an overestimation of the total fluence. The total fluence measured at insert 17A (the front insert) at the end of the irradiation period was on the order of 10^{24} - 10^{25} p/m^2 .

EIS experiments were conducted with the beam on. Although some scatter in the long-term data was observed, the polarization resistance remains fairly constant as a function of time. This observation, in combination with the finding at low fluences that R_{pol} returns to its pre-irradiation value after turning the beam off, is evidence that the proton fluence is not a major contribution to the corrosion mechanism during irradiation. Further examination of Figure 15 finds that, with the forward inserts in-beam, upon increasing the beam current to $I_t=1.0$ mA the uniform polarization resistance did not decrease significantly from the value measured at $I_t=0.40$ mA. This effect is due to spreading of the beam after striking the four front inserts. That is, the proton flux at the corrosion insert during irradiation at 1.0 mA with the four other inserts (17A and 18A-C) in front of 17B was likely equivalent to the proton flux during irradiation at 0.40 mA at the corrosion insert with no other inserts in front of 17B. After 2400 hr of irradiation (fluence = 6.5×10^{25} p/m²), experiments were conducted with the 17B insert raised approximately 0.3 to 0.6 m above the beam. As in Figure 15, only a slightly higher polarization resistance was measured when the corrosion insert was above the beam. This result is additional evidence that the effect of the 4 front inserts is to simultaneously spread the proton beam and decrease the relative proton flux near the beam center line while increasing proton flux away from the centerline. That is, had inserts 17A-18C not been in place a larger change in polarization resistance proportional to the proton flux at 1.0 mA would have been observed.

It may be noted that after approximately 1400 hours (with all inserts in place and the beam operating at 1.0 mA), the EIS data began to show evidence of a diffusion component. The effect of this diffusional impedance can be seen in the Bode magnitude data presented in Figure 16. In the frequency range of 1 to 0.04 Hz, the slope was equal to -1, which is the characteristic response of a capacitor. Below approximately 0.04 Hz the Bode magnitude data has a slope of -1/2 which is the characteristic response of a diffusional (Warburg) impedance. Therefore, the data collected after 1400 hours of immersion were modeled by a slightly different equivalent circuit than that used for data gathered at earlier immersion times. This EC is presented in Figure 8b where Z_w represents the traditional Warburg type impedance and all other elements are remain the same. As

before, the CNLS fit of the model was in excellent agreement with the experimental data (Figure 16)

4. Discussion

4.1. Water Radiolysis Products

In the analysis of gamma radiation effects on corrosion rate, authors have frequently attributed increased corrosion rates to water radiolysis products. Irradiation of water (from ionizing radiation such as proton, electron, and gamma radiation for example) results in the formation of radiolysis products, such as OH^\cdot , e^-_{aq} , HO_2^\cdot , and $\text{O}_2^{\cdot-}$ (6, 15-17), that may effect corrosion rate. These products have lifetimes which are less than a microsecond (the rate constants for recombination are greater than 10^6) before they recombine with other radiolysis products to form stable species. As a result, these "short-lived" products do not build up in the system over the course of days or weeks. For this reason any effect they may have on the corrosion rate of the sample would be anticipated to occur only while the beam was on at the proton beam / water / Alloy 718 interface(the Helmholtz layer) as they are continuously formed and annihilated at this point. Given the high reaction rate constant of these species and the velocity of the water past the Alloy 718 sample (about 1 m/s), upon turning the proton beam off, the relative concentration of short-lived products at the proton beam / water / Alloy 718 interface will be zero after a few microseconds.

The recombination of these short lived products results in the formation of stable water radiolysis products. The concentration of these stable species such as oxygen (O_2) and hydrogen peroxide (H_2O_2) will gradually increase with increasing fluence (time). In the case of O_2 and H_2O_2 , these long-lived radiolysis products are cathodic reactants and, therefore, will increase cathodically limited corrosion rates and OCP's. Here hydrogen water chemistry was used to mitigate the formation of this species. After 143 days of irradiation the peroxide concentration was less than 0.29 mole/m^3 . However, it is possible that the concentration of long-lived products will be higher than their bulk values at the proton beam / water / Alloy 718 interface. If the decrease in

corrosion rate observed during proton irradiation owed primarily to an increase in concentration of radiolysis products (long-lived or short-lived) at the proton beam / water / Alloy 718 interface, the post-irradiation corrosion rate should return to its pre-irradiation value in less than a second. However, the decay of R_{pol} back to its pre-beam value took more than 20 minutes (Figure 11). Therefore, it is unlikely that radiolysis products played any tangible role in the observed increase in Alloy 718 corrosion rates.

4.2. Direct Sample Particle Beam Interactions

Another proton beam effect that must be considered is heating, caused by energy deposition in the Alloy 718 sample. To estimate the peak surface temperatures for the in-beam corrosion samples, thermal-hydraulic calculations were performed. These calculations were based on the flow rate in each tube, inlet water temperature, sample thickness and material, and power density variations along the sample and tube lengths. With the exception of power density, values for these parameters can be found in Sections 2.1 and 2.2. The power density varied with beam current for a specific beam profile (Equation 1). For the Gaussian beam with a sigma of 1.5 cm, the peak power density in the Alloy 718 sample at 0.40 mA, for example, was $4.93 \times 10^8 \text{ W/m}^3$ while the average power density over the sample was $1.38 \times 10^8 \text{ W/m}^3$. Calculations were performed at 13 sample and tube node locations. At each location, the sample and tube temperatures were calculated using the local water temperature, heat transfer coefficient, and power deposition in the sample and tube. Experimentally, thermocouples were brazed to the outside of the cooling water tube, that surrounded the Alloy 718 probes, at the midpoint. For completeness, a detailed calculation of thermocouple temperature, assuming the beam was centered at the midpoint location was also performed.

Table 2 shows the calculated Alloy 718, tube, and thermocouple temperatures for beam currents of 0.001, 0.01, 0.04, 0.10, and 0.40 mA. The water inlet temperature used in these calculations was 20 °C for all currents even though the actual water temperature varied a few degrees from this value. The calculated peak sample surface temperatures ranged from slightly above water temperature at a proton beam current of 0.001 mA up to 122.9 °C at 0.40 mA. The

corresponding peak temperature for the inner surface of the flow tube was 91.7 °C at 0.40 mA, while the calculated thermocouple temperature attached to the outside of the tube was 143.9 °C. Table 2 also shows the sensitivity of temperature to beam position. For example, at 0.40 mA, a position 2.5 cm from beam centerline has a peak sample surface temperature of only 52.7 °C versus the 122.9 °C at the beam centerline. Therefore, when comparing the calculated thermocouple temperatures to the experimental values, beam position must be considered. That is, as the beam was not centered on the midpoint of the tube the thermocouples are expected to measure lower temperatures than the maximum calculated thermocouple temperatures given in Table 2. Moreover, the steering thermocouples (referred to in Section 1.1) located the beam XY position as approximately -0.4, -0.1 cm relative to the tube center. Future hot-cell work will include autoradiographs of the tube to more accurately determine the position of the proton beam with respect to the tube thermocouples.

Although temperature increases the kinetics of the anodic reaction, for passive metals (such as Alloy 718 in high purity water) corrosion rate at the OCP is controlled by the passive film. To investigate the role of sample temperature on corrosion rate, potentiodynamic polarization curves for Alloy 718 in pH 7 5.0×10^{-4} mole/m³ boric acid / 5.0×10^{-5} mole/m³ sodium borate buffer solution were generated at 22° C and 74° C +/- 2° (Figure 17; reference electrode potentials were temperature corrected in accordance with Ives and Janz(18)). In borate buffer solution, Alloy 718 is passive. Therefore, corrosion rate at the OCP is controlled by the passive film as in high temperature / high purity water. A higher temperature was not chosen, as oxygen depletion of the solution occurs at temperatures greater than 80° C for systems open to the atmosphere. As these polarization curves were generated in an open cell, corrosion rate would reach a maximum at 80° C. As a conservative approximation, the results from potentiodynamic testing at 74° C will be compared with those obtained during irradiation at 0.10 mA. Thus, the described temperature limit is of little consequence as 74° C is in the range of the calculated peak surface temperature for the in-beam sample between beam currents of 0.10 and 0.4 mA.

From the potentiodynamic polarization curves we find that the ratio of i_{corr} at 74° C to i_{corr} at 22° C was 1.33 (2.8×10^{-4} A/m² and 2.1×10^{-4} A/m² respectively). That is, a 50° C increase in sample temperature produced a 33% increase in corrosion rate. For the in-beam sample, the ratio of $1/R_{\text{pol}}^*$ measured during irradiation at 0.10 mA (46° C) to that measured with the beam off (15° C) was 180 ($1/(9.3 \text{ ohm} \cdot \text{m}^2)$ and $1/(1.7 \times 10^3 \text{ ohm} \cdot \text{m}^2)$ respectively, Figure 17). Although, the calculated peak surface temperature of the in-beam sample is 28° C below the temperature used in the potentiodynamic polarization experiment, the corrosion rate of the in-beam sample increased by 2 orders of magnitude during irradiation. Therefore, while heating of the in-beam sample due to energy deposition from the proton beam occurred, its contribution to the observed decrease in corrosion rate during irradiation was small.

In addition to temperature effects, the proton beam may also cause radiation damage in the sample. Radiation damage may be divided into two basic categories, physical damage and changes in electrical and optical properties. Physical damage to the passive film such as displacement, amorphization, Frenkel defects, sputtering, implantation, etc. generally occurs at lower particle energies (< 10 MeV) and may result from ballistic impact of the particle with the material or from the indirect transfer of kinetic energy. Although recoiling of the nucleus after a spallation event may cause some local distortions in the oxide, these passive films have no long range order, therefore, there is no effect on a lattice *per se*. Physical damage in the metal, such as proton / neutron induced segregation resulting in chromium depleted zones, is not ruled out. Typically, however, the effects of segregation are not observed until higher fluences and, therefore, this does not explain the "instantaneous" changes in polarization resistance observed here.

At higher particle energies (> 10 MeV) the particle causes continuous electronic excitations in the material as it passes through it. For insulators and semiconductors (such as passive oxides) this electronic excitation may result (indirectly) in the promotion of valence electrons to the conduction band. Although many of the electron-hole pairs that form in this manner recombine instantly (geminate recombination), those which escape this phenomena are free to migrate in an

* R_{pol} is inversely proportion to the i_{corr} . Both R_{pol} and i_{corr} are determined at the OCP.

electric field. This is known as radiation induced conductivity (RIC) and accounts for the relatively high conductivities observed in otherwise insulating materials such as Al_2O_3 (19) and MgAl_2O_4 spinel(20) during high energy proton irradiation. It has been shown that uv irradiation effects the corrosion properties of 304 and 316 stainless steel in a similar manner to the proton effect observed here(21, 22). The passive oxide that forms on 304 and 316 SS is semiconducting in nature (as is the oxide on Alloy 718). Currently we are exploring the use of Mott-Schottky analysis(23) to determine if a change in donor concentration occurs in the Alloy 718 oxide as well as quantify the amount of increase. Results of this work will be presented in future publications.

5. Conclusions

A seminal experimental effort to characterize the corrosion rates of materials in spallation neutron source target cooling loops has been conducted at the Los Alamos Neutron Science Center. Electrochemical impedance spectroscopy has been demonstrated to be a powerful method for measuring the real-time corrosion rates of materials in high purity water during proton irradiation. For 800 MeV proton irradiation, EIS found that the corrosion rate of Alloy 718 increased exponentially with increasing beam current. Over the range of 0.001 to 0.40 mA the corrosion rate increased from 0.041×10^{-6} m/yr. to 3.1×10^{-6} m/yr. assuming uniform corrosion over the sample surface. These rates may be an order of magnitude higher when proton flux is considered as the proton beam had a Gaussian distribution where 2 σ irradiated approximately 25% of the sample surface. The observed increase in corrosion rate during proton irradiation was found to be temporary for low proton fluences although the decay back to pre-irradiation values was slow (on the order of 3 hrs). Although the mechanism by which proton radiation decreases corrosion rate is not entirely understood, this finding rules out water radiolysis as a major contributor.

Acknowledgments

All work on this project was performed by the University of California under the auspices of the US Department of Energy contract W-7405-ENG-36. The authors would like to thank Laurie Waters and the continued support of the APT project office; Walt Sommer, Stuart Maloy, and Luke Daemen for helpful discussions; Richard Werbeck, Bob Brown, Eugene Zimmerman and the rest of the LANSCE-7 group for their engineering expertise in the fabrication of the corrosion insert; Greg Chandler (SRS) for some of the data collection; and Len Reed and Paul Lavoie of INTA (Santa Clara CA) for the design and fabrication of the in-beam corrosion probes.

References

- [1] R. S. Lillard, D. P. Butt, Using Solution Resistivity as an Estimate of Tungsten Corrosion in Spallation Neutron Target Cooling loops, Los Alamos National Laboratory, LAUR 97-561 (1997).
- [2] W. Sommer, S. Maloy, M. Zaslowski, in 2nd International Workshop on Spallation Materials Technology, Ancona, Italy, 1997.
- [3] S. Maloy, et al., in TMS Degradation of Materials in Nuclear Power System Water, Newport Beach, 1999, TMS.
- [4] M. Simnad, R. Smoluchowski, Physics Review, 98 (1955) 1891.
- [5] M. Simnad, R. Smoluchowski, Physics Review, 99 (1955) 1961.
- [6] F. E. Hoyer, in Fourth International Congress on Metallic Corrosion, N. E. Hamner (Ed) Amsterdam, 1972, NACE, .
- [7] R. S. Lillard, D. P. Butt, accepted for publication in Materials Characterization, (1999) .
- [8] M. Sluyters-Renbach, J. H. Sluyters, Electroanalytical Chemistry, 4 (1) (1970) 1.
- [9] J. R. MacDonald, Impedance Spectroscopy, Wiley Publishing, New York, 1987.
- [10] D. D. MacDonald, in: Electrochemical Corrosion Testing, ASTM STP 727, F. Mansfeld, U. Bertocci (Eds), ASTM, Philadelphia, 1981, p. 110.
- [11] J. E. B. Randles, Discussions of the Faraday Society, 1 (1947) 11.
- [12] W. F. Sommer, APT Materials Safety Experiments Technical Report, Los Alamos National Laboratory, LAUR-93-2850 (1993).
- [13] F. Mansfeld, in: Electrochemical Techniques, R. Baboian (Ed), NACE, Houston, 1986, p. 67.
- [14] R. S. Lillard, Corrosion Rates Alloy 718 as a Function of Beam Current, Los Alamos National Laboratory, MST6-99-039 (1999).
- [15] S. M. Pimblott, J. A. LaVerne, Radiation Research, 129 (1992) 265.
- [16] W. G. Burns, P. B. Moore, Radiation Effects, 30 (1976) 233.

- [17] W. G. Burns, W. R. Marsh, *Journal of the Chemical Society, Faraday Transactions 1*, 77 (1981) 197.
- [18] D. J. G. Ives, G. J. Janz, *Reference Electrodes Theory and Practice*, Academy Press, NY, 1961.
- [19] G. P. Pells, *Journal of Nuclear Materials*, 184 (1991) 183.
- [20] G. P. Pells, *Journal of Nuclear Materials*, 184 (1991) 177.
- [21] E. Sikora, C. Breslin, J. Sikora, D. D. MacDonald, in: *Critical Factors in Localized Corrosion III*, PV95-15, P. M. Natishan, R. G. Kelly, G. S. Frankel, R. C. Newman (Eds), ECS, Pennington, 1995, p. 344.
- [22] C. B. Breslin, D. D. MacDonald, E. Sikora, J. Sikora, *Electrochimica Acta*, 42 (1997) 137.
- [23] P. Schmuki, H. Bohni, *Journal of the Electrochemical Society*, 139 (1992) 1908.

Tables

Table 1 Effect of 260 MeV protons on the open circuit potential of tungsten (from ref. [4]).

| Sample Number | Proton Fluence (p/m²) | Change in Electrode Potential (mV) |
|----------------------|---|---|
| 0 | 0 | 0 |
| 1 | 1.8×10^{19} | 39 |
| 2 | 6.8×10^{19} | 47 |
| 3 | 2.2×10^{20} | 84 |

Table 2 Calculated Alloy 718, tube, and thermocouple temperatures vs beam current. All temperatures are in °C. Measured thermocouple temperatures are also presented.

| | 0.001 (mA) | 0.01 (mA) | 0.04 (mA) | 0.10 (mA) | 0.40 (mA) |
|--|-----------------------------|----------------------------|----------------------------|----------------------------|----------------------------|
| Water temp at peak location | 20.0 | 20.1 | 20.3 | 20.8 | 23.1 |
| Alloy 718 surface temperatures | | | | | |
| Peak at beam centerline | 20.3 | 22.6 | 30.3 | 45.7 | 122.9 |
| 1.5 cm from peak (radial) | 20.2 | 21.7 | 26.7 | 36.7 | 87.0 |
| 2.5 cm from peak (radial) | 20.1 | 20.8 | 23.3 | 38.2 | 52.7 |
| Average on sides of sample | 20.1 | 20.8 | 23.0 | 27.6 | 50.3 |
| Tube inner surface temperatures | | | | | |
| Peak at beam centerline | 20.2 | 21.8 | 27.2 | 37.9 | 91.7 |
| 1.5 cm from peak (radial) | 20.1 | 21.2 | 24.6 | 31.6 | 66.4 |
| 2.5 cm from peak (radial) | 20.1 | 20.6 | 22.3 | 25.7 | 42.6 |
| Calculated thermocouple temp. | 20.3 | 23.1 | 32.4 | 51.0 | 143.9 |
| Measured thermocouple temp. | 15-18 | 18-21 | 21-22 | 24-27 | 50-67 |

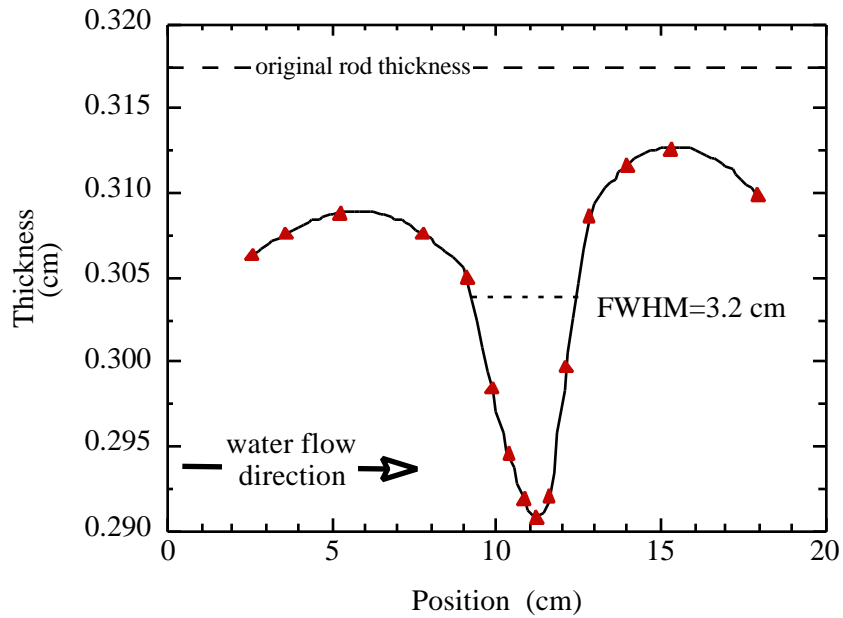


Figure 1 Thickness changes in a 0.318 cm diameter tungsten rod after proton irradiation at 1.0 mA for 2 months (adapted from ref 2).

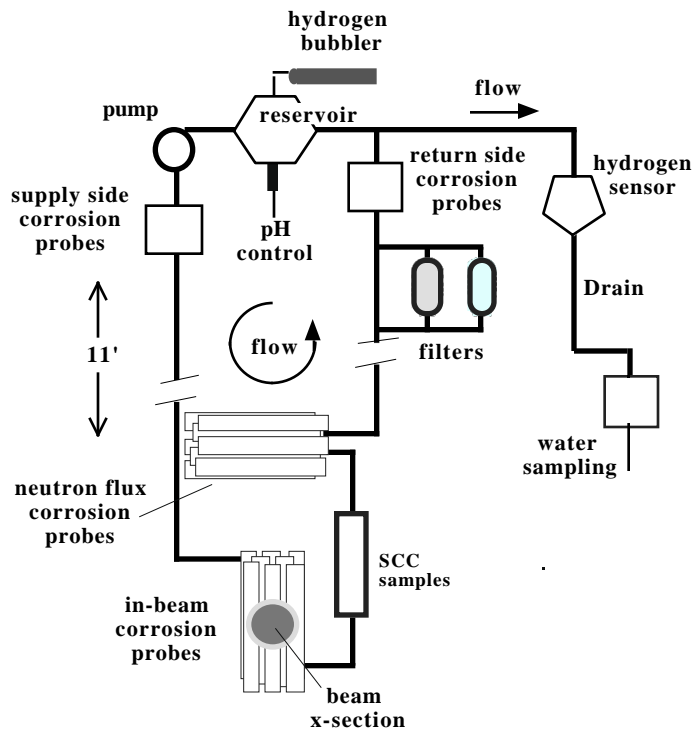


Figure 2 A diagram representing the corrosion water system at the LANSCE A6 Target Station. This system was used to measure the real-time corrosion rates of materials during proton irradiation. Only the results from the in-beam corrosion loop are discussed here.

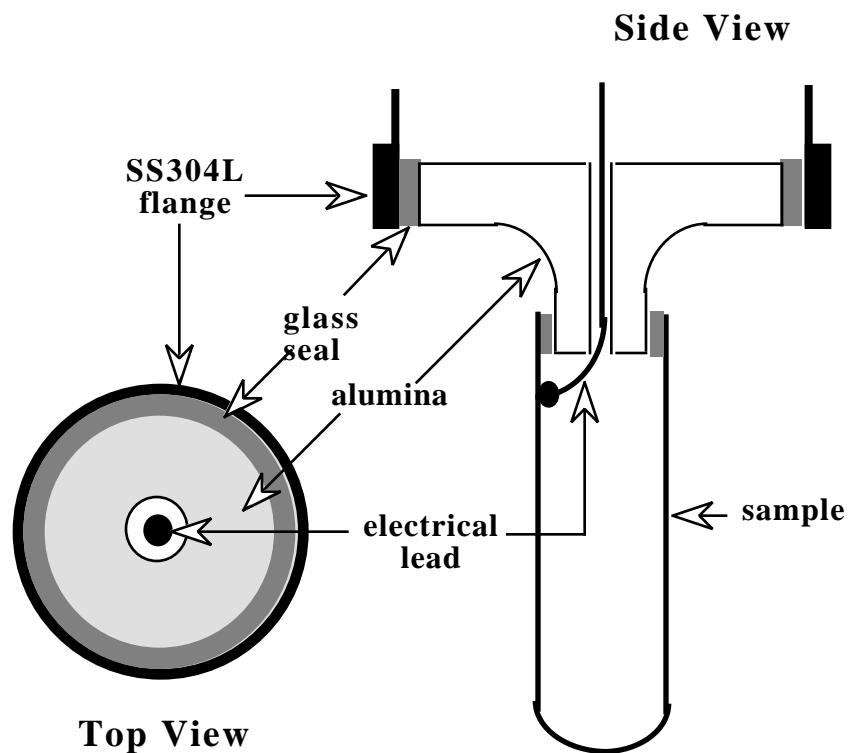


Figure 3a A diagram depicting a corrosion probe used to electrically isolate the corrosion samples from the cooling water system. Samples were mounted on the alumina by means of a compression seal.

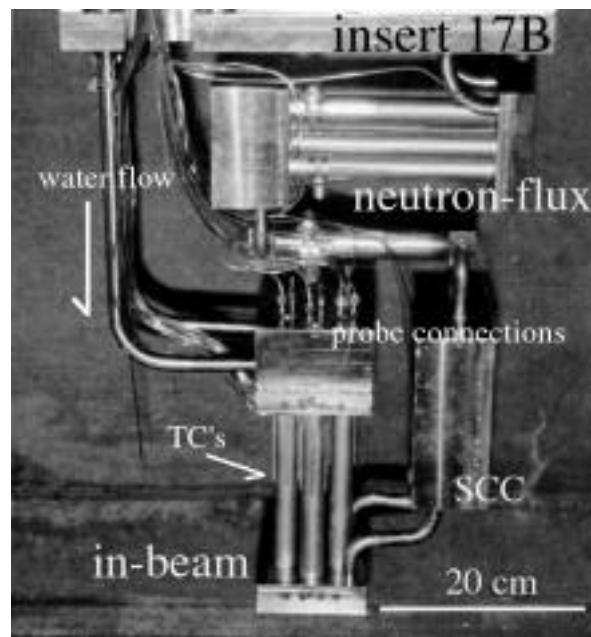


Figure 3b A photograph of the water manifold (insert 17B) that contained the in-beam corrosion probes prior to being set in place at the A6 Target Station. The proton beam is perpendicular to the page.

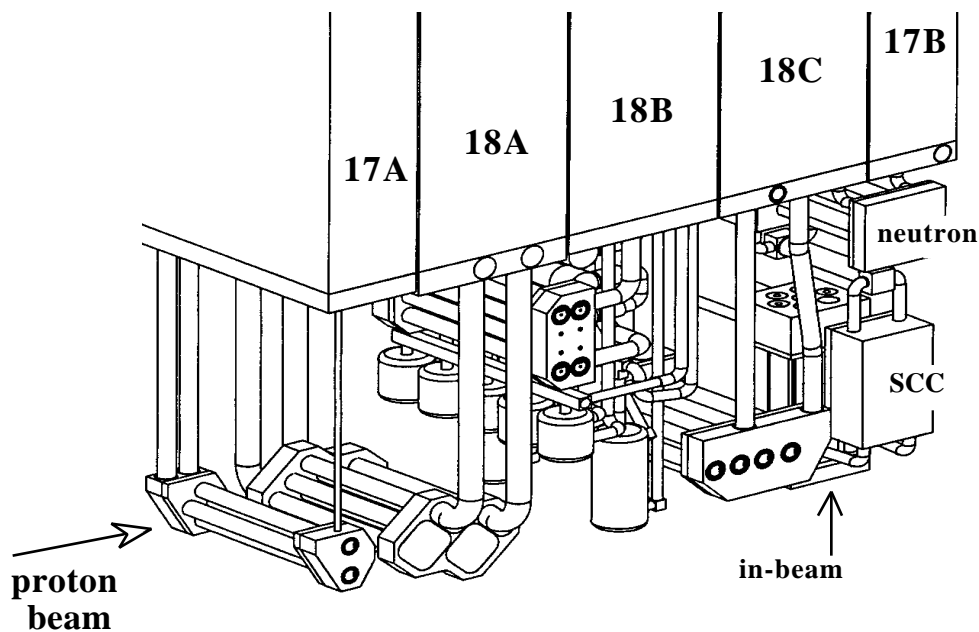


Figure 4 A diagram representing the A6 Target Station at LANSCE and all of the materials irradiation inserts. Early in-beam data reported on in this paper were collected with inserts 17A-18C removed from the beam path. At later times, inserts 17A-18C were placed in-beam as shown in this figure.

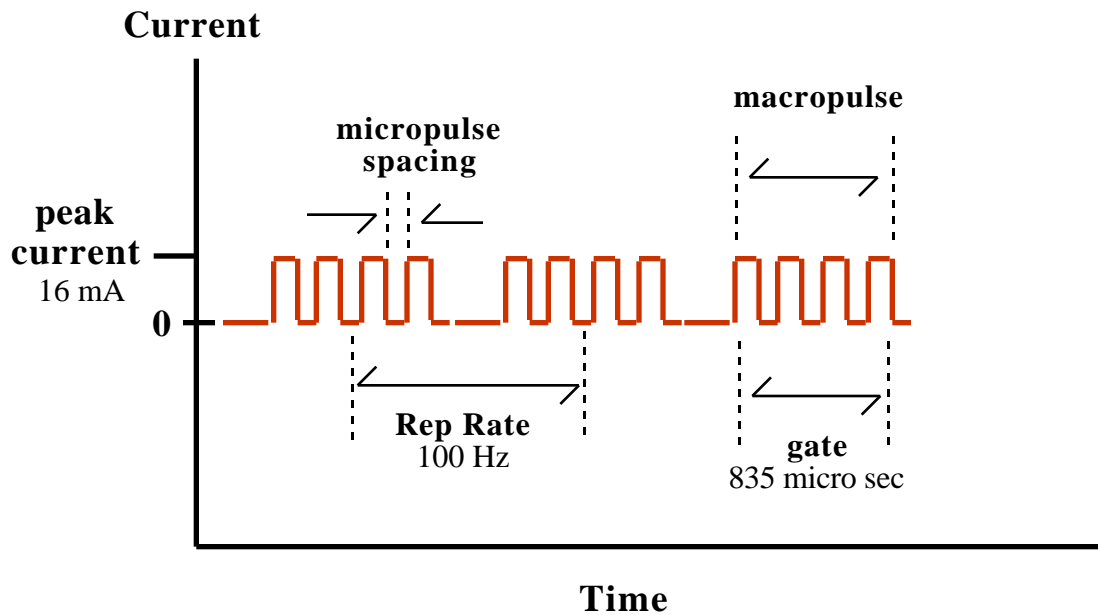


Figure 5 A diagram representing the duty cycle for the beam at the LANSCE A6 target station.

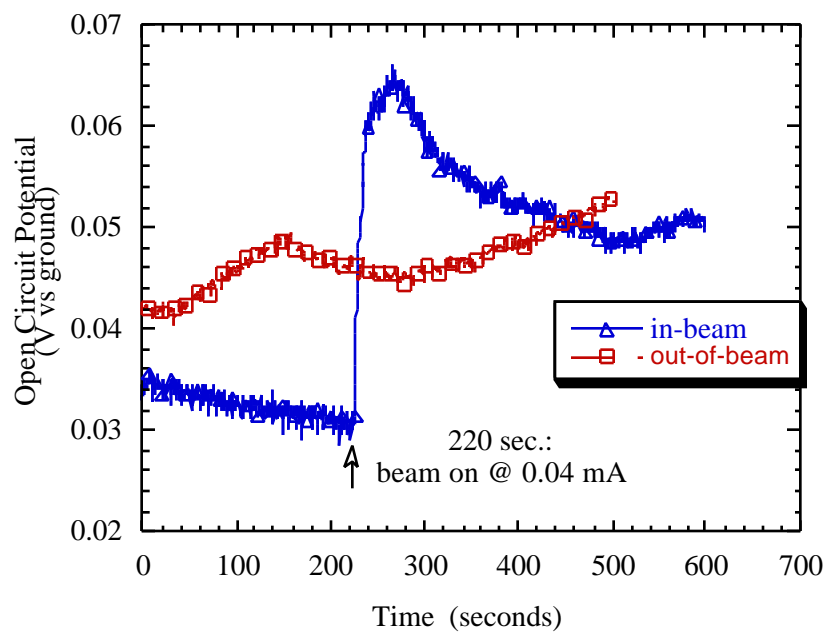


Figure 6 Open circuit potential of the in-beam and out-of-beam alloy 718 samples before and during proton irradiation. Potential was measured with respect to ground (that is, the stainless steel water system). For clarity not all data points are shown.

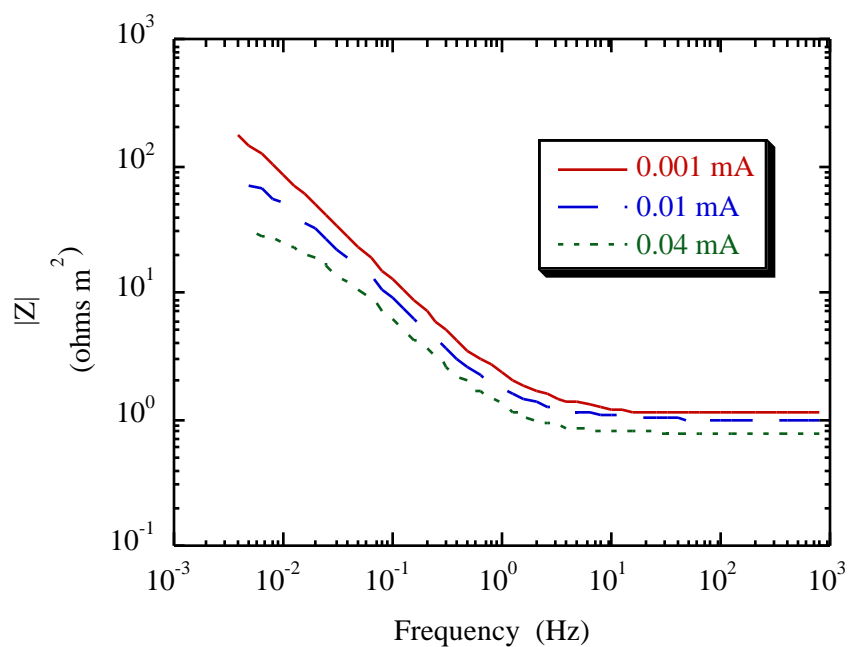


Figure 7a Bode magnitude plots from the 718 sample during proton irradiation at proton beam currents of 0.001, 0.01, and 0.40 mA. The area normalization assumes uniform dissolution across the sample surface.

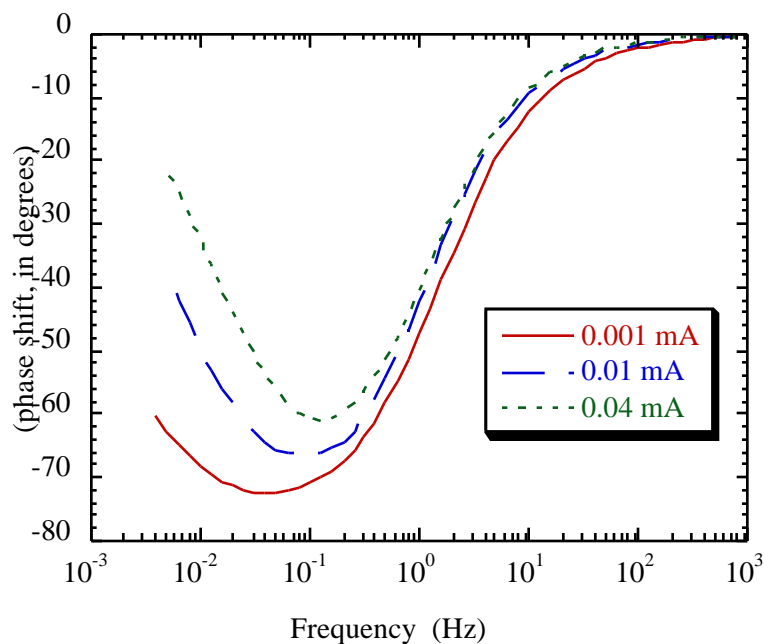


Figure 7b Bode phase plots from the 718 sample during proton irradiation at proton beam currents of 0.001, 0.01, and 0.40 mA.

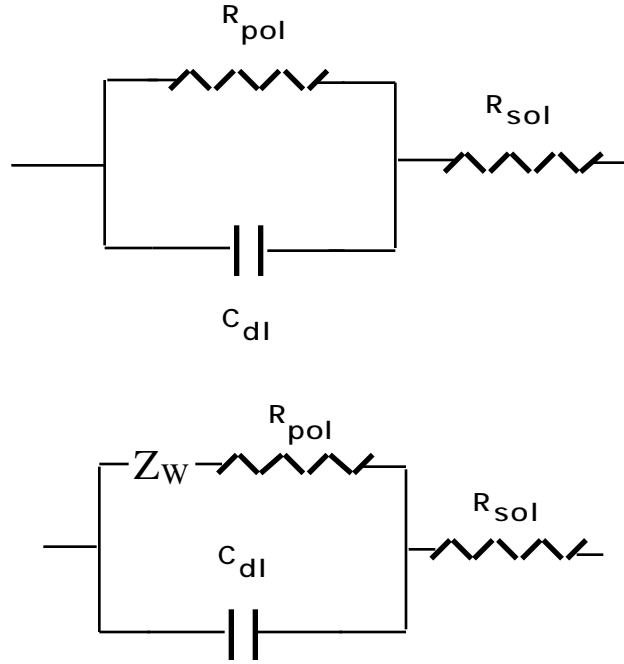


Figure 8 Equivalent circuit models used in complex non-linear least squares fitting of the EIS in (a): R_{pol} represents the polarization resistance and is inversely proportional to corrosion rate, C_{dl} represents the double layer capacitance, and R_{sol} represents the geometric solution resistance and (b) Z_w represents a diffusional (Warburg) type impedance.

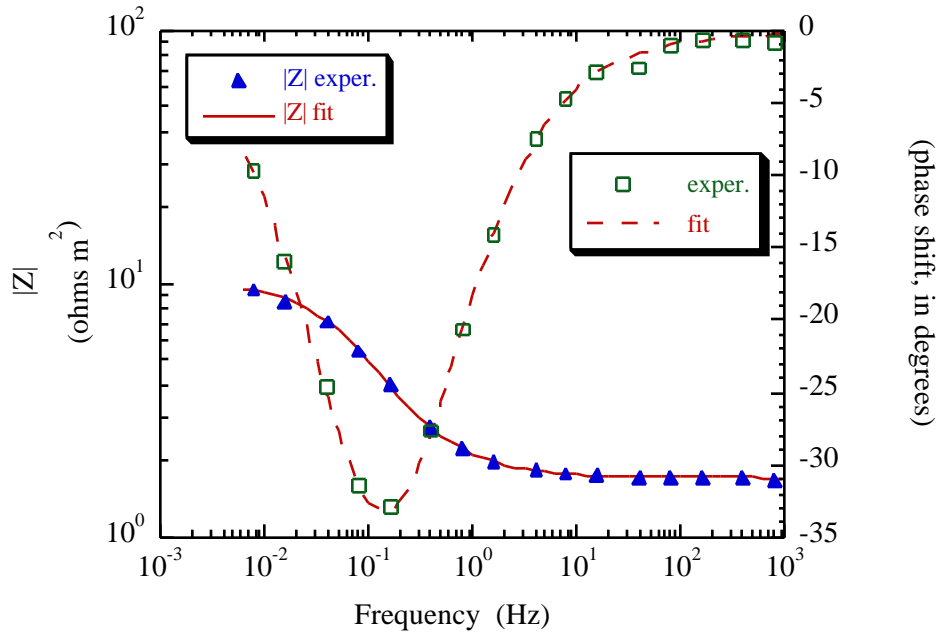


Figure 9 Bode magnitude and phase data from the in-beam 718 sample during irradiation at 0.40 mA and the CNLS fit of the data to the equivalent circuit shown in Figure 8a. For clarity, not all experimental data are shown. As in Figure 6a, the area normalization assumes uniform dissolution across the sample surface.

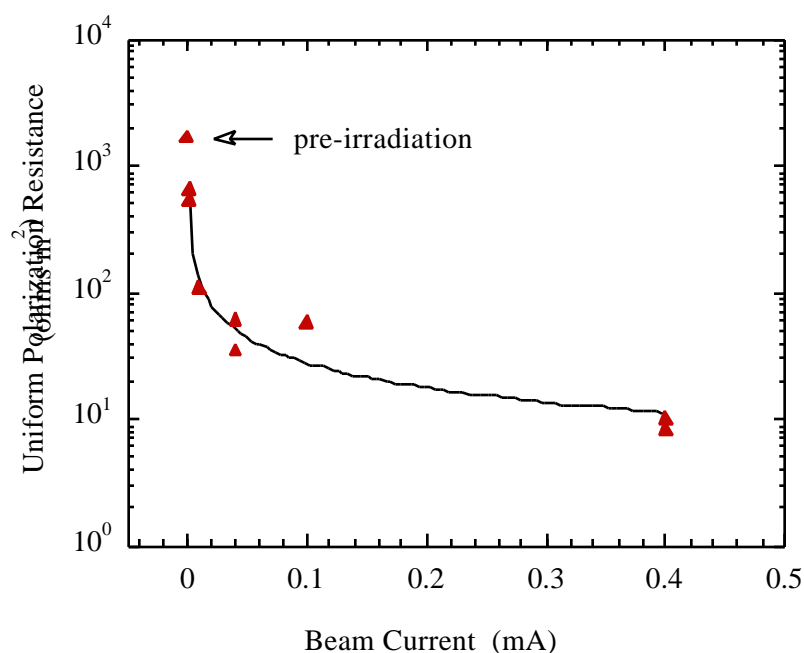


Figure 10 Uniform polarization resistance for alloy 718 as a function of beam current. The area normalization assumes uniform corrosion across the sample surface. Therefore, the polarization resistance is referred to as "uniform".

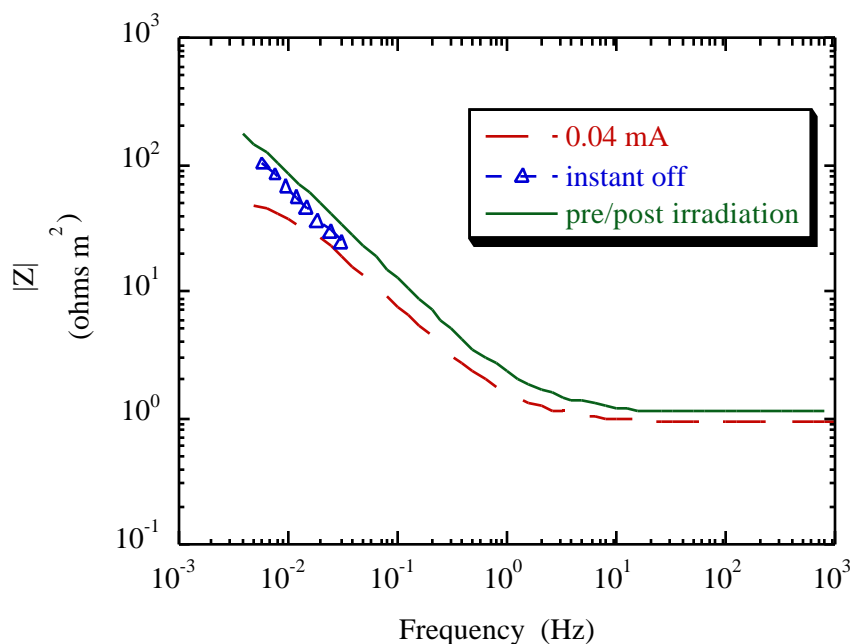


Figure 11 Bode magnitude data for 718 before and 3 hours after irradiation at 0.040 mA, during irradiation at 0.040 mA, and immediately after the beam was turned off ("instant off"). The slope of the instant off data is less than -1 indicating the impedance is changing with time. As in Figure 6a, the area normalization assumes uniform dissolution across the sample surface.

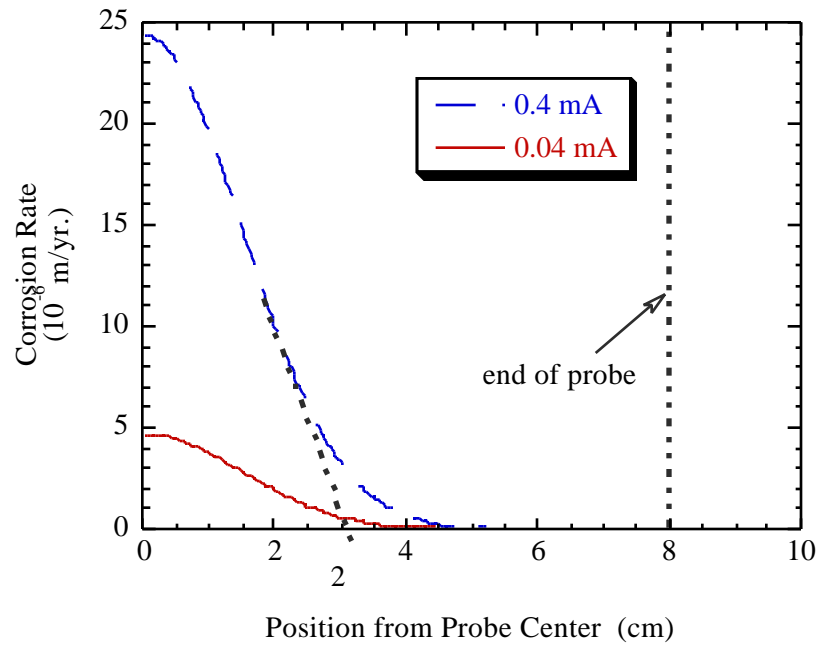


Figure 12 Calculated corrosion rate as a function of radial distance from the probe center (which was approximately equal to the beam center) as calculated from Equations 3-6. These profiles would be observed if corrosion rate was a function of proton flux of the incident proton beam.

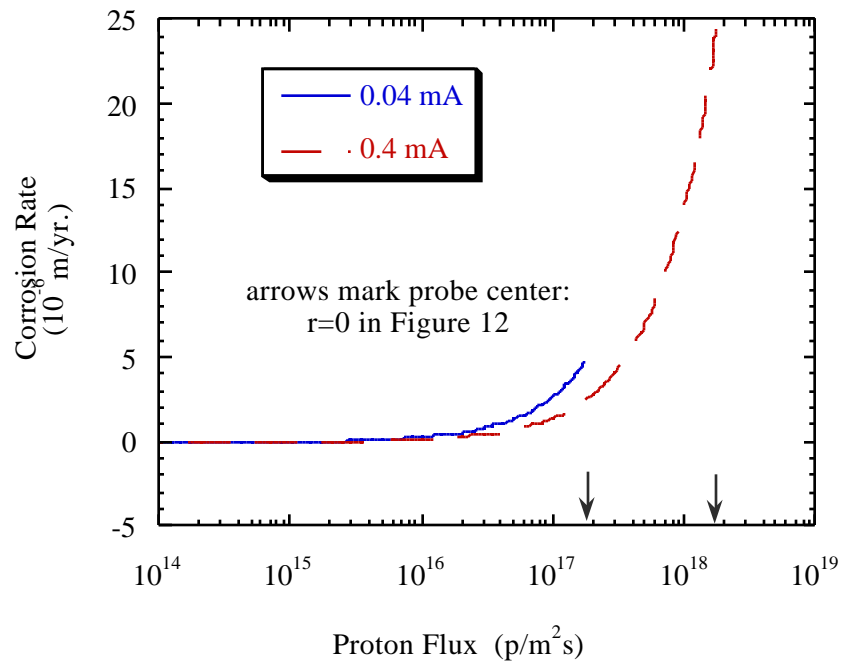


Figure 13 Calculated corrosion rate from the in-beam 718 sample as a function of proton flux (From Figure 12). Proton flux was calculated from Equation 1 for proton beam currents (I_T) of 0.04 and 0.4 mA. The probe center was approximately equal to the beam center

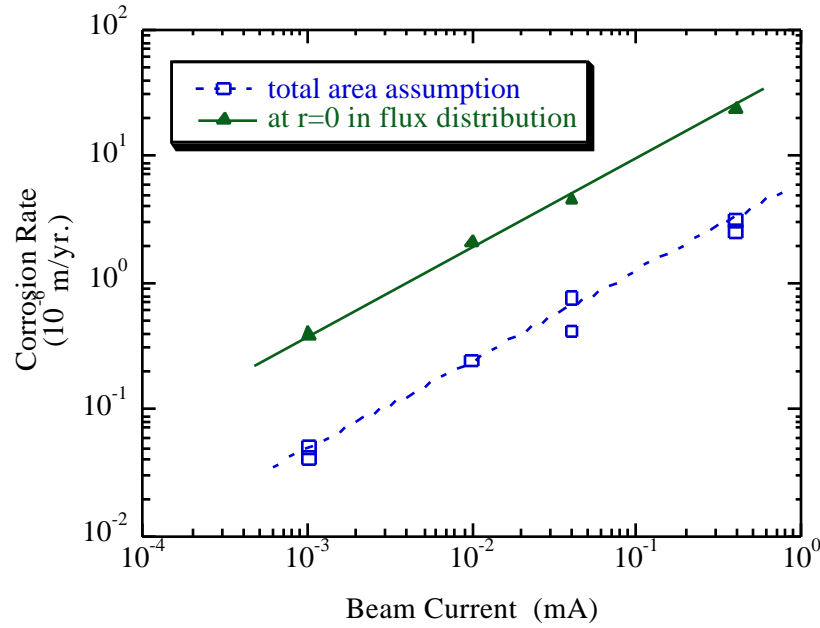


Figure 14 Corrosion rate from the in-beam 718 sample as a function of proton beam current. The rates are calculated for two assumptions concerning the corroding area: 1) corrosion rate was uniform over the entire sample surface and 2) corrosion rate as a function of proton flux, Equations 3-6 (@ $r=0$ in Figure 12, or at peak flux in Figure 13).

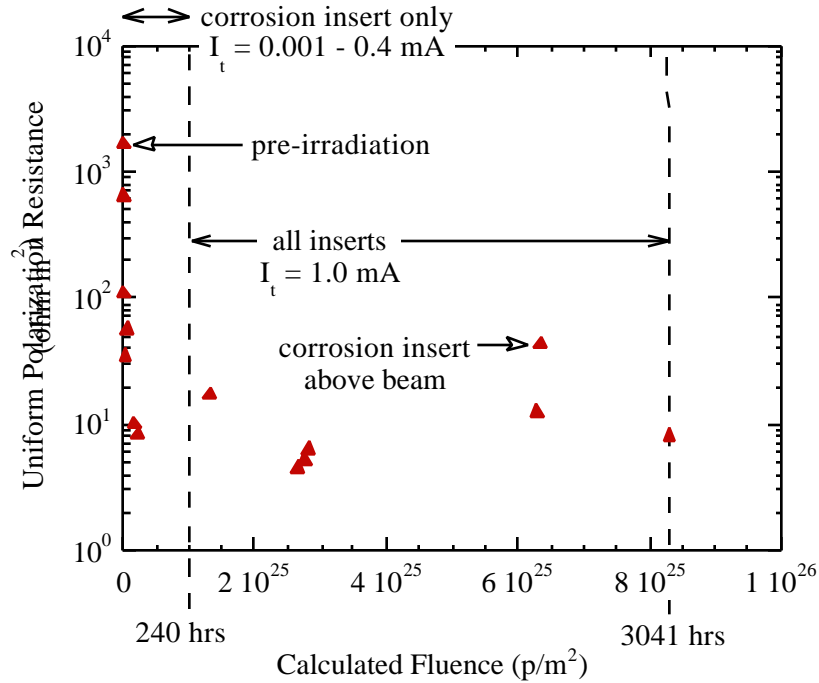


Figure 15 Uniform polarization resistance from the in-beam Alloy 718 sample as a function of proton fluence. The first 240 hrs of data were collected with all other inserts removed from the beam path. During the remainder of the irradiation all inserts were in place.

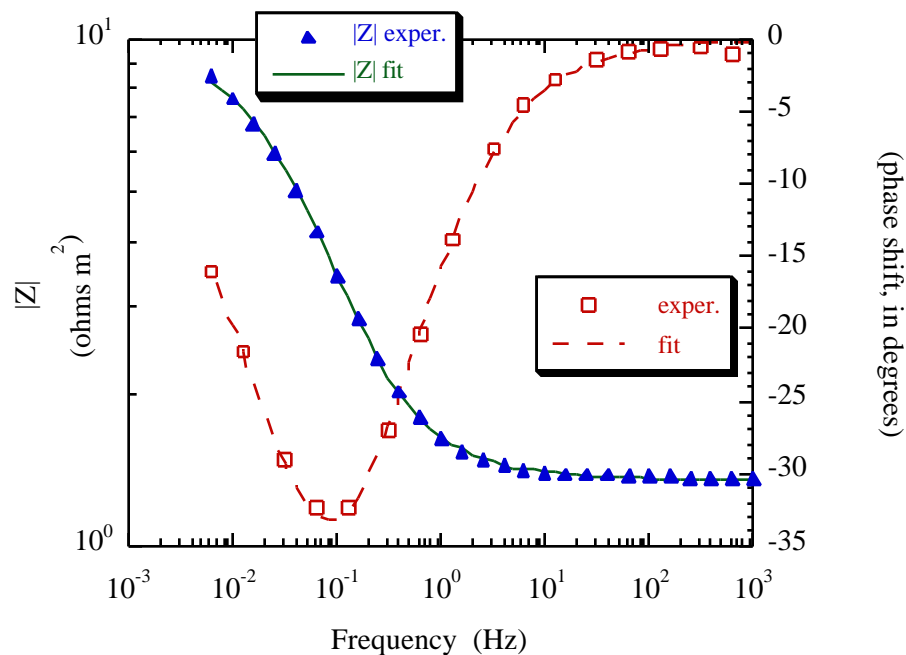


Figure 16 Typical EIS data for alloy 718 after 1440 hrs of irradiation. The Warburg impedance is noted by the change in slope at 0.04 Hz from -1 at higher frequencies to -1/2 at lower frequencies. Note, only 20% of the experimental data is shown for clarity.

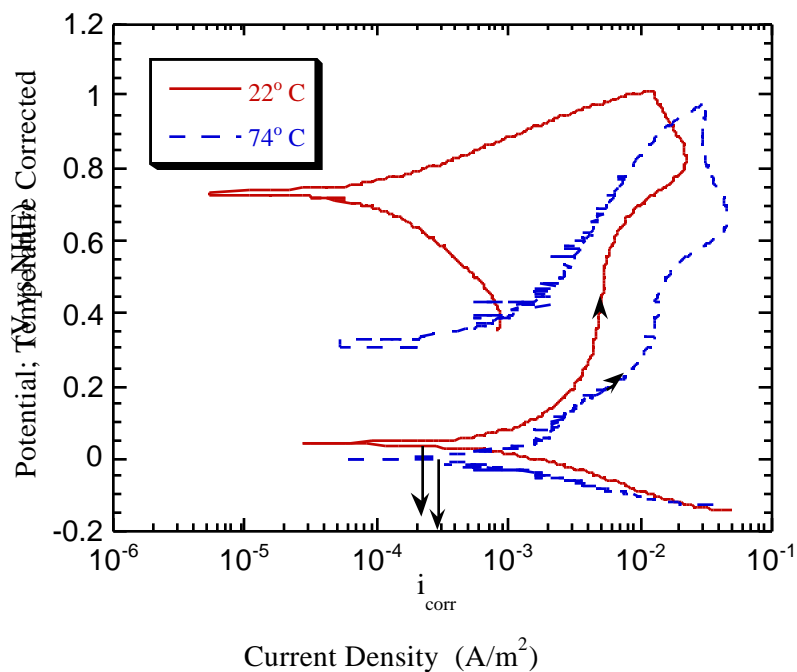


Figure 17 Potentiodynamic polarization curves for alloy 718 in borate buffer pH 7.2 at 22° C and 74° C. Potentials were measured with a mercury/mercury-sulfate reference electrode and temperature corrected in accordance with Ives & Janz (18).